Unique orientation of 1D and 2D nanoparticle assemblies confined in smectic topological defects

Haifa Jeridi, Jean de Dieu Niyonzima, Charbel Sakr, Amine Missaoui, Sharif Shahini, Alina Vlad, Alessandro Coati, Nicolas Goubet, Sébastien Royer, Ian Vickridge, et al.

Cite this: DOI: 00.0000/xxxxxxxxxx

Unique orientation of 1D and 2D nanoparticle arrays confined in smectic topological defects †

Hayfa Jeridi,[a,b] Jean de Dieu Niyonzima,[a,c] Charbel Sakr,[a] Amine Missaoui,[a] Sharif Shahini,[a,d] Alina Vlad,[e] Alessandro Coati,[e] Nicolas Goubet,[f] Sebastien Royer,[a] Ian Vickridge,[a] Michel Goldmann,[a,e] Doru Constantin,[g] Yves Garreau,[e,h] David Babonneau,[i] Bernard Croset,[a] Bruno Gallas,[a] Emmanuel Lhuillier,[a] and Emmanuelle Lacaze*[a]

Received Date
Accepted Date

DOI: 00.0000/xxxxxxxxxx

New collective optical properties emerge nowadays with organized and oriented arrays of close packed semiconducting and metallic nanoparticles (NPs). However, it is still challenging to obtain NP assemblies everywhere similar on a given sample and most importantly sharing a unique common orientation that would guarantee a unique behavior everywhere on the sample. In this context, combining Optical Microscopy, Fluorescence Microscopy and synchrotron-based Grazing Incidence X-ray scattering (GISAXS) of assemblies of gold nanospheres and of fluorescent nanorods, we study the interactions between NPs and liquid crystal smectic topological defects that can ultimately lead to unique NP orientation. We demonstrate that arrays of one-dimensional - 1D (dislocations) and two-dimensional - 2D (grain boundaries) topological defects oriented along one single direction confine, organize in close packed networks but also orient both single nanorods and NP networks along the same direction. Through the comparison between smectic films associated with different kinds of topological defects, we highlight that the coupling between the NP ligands and the smectic layers below the grain boundaries is necessary to allow for fixed NP orientation. This is in contrast with 1D defects where the induced orientation of the NPs is intrinsically induced by the confinement, independently of the ligand nature. We thus succeeded to achieve fixed polarization of assemblies of single photon emitters in defects. For gold nanospheres confined in grain boundaries, a strict orientation of hexagonal networks has been obtained with the $\langle 10 \rangle$ direction strictly parallel to the defects. With such close-packed and oriented NPs, new collective properties are now foreseen.

1 Introduction

A long range control of orientation and organization of metallic nanoparticles (NPs) would lead to anisotropic Localized Surface Plasmon Resonnance (LSPR) becoming strictly controlled by incident light polarization when NPs are anisotropic or are assembled within anisotropic organizations.[1–4] For fluorescent anisotropic NPs, controlled polarization of the emitted light would be generated.[2,5] When NPs are close-packed in a well-defined organization, collective properties can even emerge. In metallic NP chains there are delocalized plasmonic bands.[6,7] It has been shown recently that well-defined one-dimensional (1D) packing of fluorescent NPs can induce long range (up to 600 nm) Fluorescence Resonance Energy Transfer (FRET).[8] The extension of this kind of collective features at two dimensions (2D) is challenging since a control of NP orientation and organization is required at 2D.[9] Lithography is an efficient tool to build long-range well-defined networks of NPs, however without real close-packing of NPs. For such a purpose colloidal NPs can be used. A number of recent works has been devoted to the study of NP assemblies obtained by controlled solvent evaporation.[10,11] It remains difficult to ensure a single orientation for the corresponding networks but recent achievements with microfluidic devices appear promising.[12] Moreover when nanorods are concerned, slow evaporation favours membrane formation with nanorods perpendicular to the substrate[13–15] whereas for a number of optical properties nanorods parallel to the substrate might be preferred. To achieve formation of oriented networks of close-packed NPs, template-assisted colloidal self-assembly has been developed since a few years. When the template is provided by the substrate beautiful arrays of NPs have been obtained but the width of each assembly usually remains limited.[9,16,17] For orientation control, liquid crystals (LC) are an interesting alternative due to their intrin-

[a] CNRS, Institut des Nanosciences de Paris, INSP, Sorbonne UniversitÃľ, F-75005 Paris, France; Tel: +33 144 274 654; E-mail: emmanuelle.lacaze@insp.jussieu.fr
[b] OMNES Education Research center, ECE Paris, 37 quai de Grenelle, 75015 Paris, France.
[c] Physics department, School of Science, College of Science and Technology, University of Rwanda, Po.Box: 3900 Kigali, Rwanda.
[d] University of Luxembourg, Luxembourg, L-1511, Luxembourg.
[e] Synchrotron SOLEIL, BP 48, L'Orme des Merisiers, 91192 Gif sur Yvette Cedex, France.
[f] CNRS, Sorbonne UniversitÃľ, Laboratoire de la MolÃľcule aux Nano-objets; RÃľactivitÃľ, Interactions et Spectroscopies MONARIS, 4 Pl Jussieu, Case Co, F-75005 Paris, France.
[g] UniversitÃľ de Strasbourg, Institut Charles Sadron, CNRS UPR022, 67034 Strasbourg Cedex, France.
[h] UniversitÃľ de Paris, Laboratoire MatÃľriaux et PhÃľnomÃĺnes Quantiques, CNRS, F-75013 Paris, France.
[i] Departement Physique et Mecanique des Materiaux, Institut P', UPR 3346 CNRS, UniversitÃľ de Poitiers SP2MI, TSA 41123, 86073 Poitiers cedex 9, France.
† Electronic Supplementary Information (ESI) available: See DOI

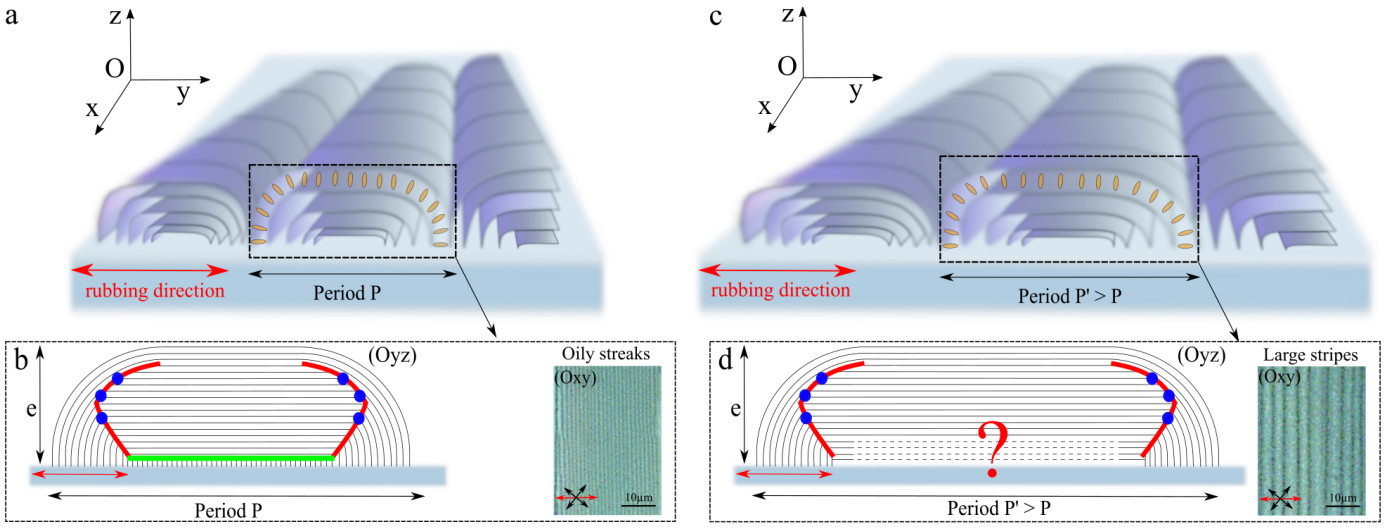

Fig. 1 (a)-(c) Simplified 3D schematic of oily streak and large stripe respectively where smectic layers are curved in flattened hemicylinders with the molecular orientation shown in yellow. (b)-(d) Crossed sectional views ((Oyz) plane) of hemicylinders depicting in (b) oily streak texture with superimposed smectic layers, two rotating grain boundaries (RGB) in red of height around 80 nm, including six linear dislocations in blue and a 2D central defect in green; (d) large stripe texture with the same expected architecture at the edges (RGB and the six linear dislocations) but with a larger central zone (larger periodicity) of unknown structure close to the substrate. The POM pictures in reflection show the top view of both textures ((Oxy) plane) of similar thickness ($e \approx 200$ nm), each stripe corresponding to one hemicylinder.

sic anisotropy.[18] Anisotropic NPs can be oriented by the nematic director.[19–21]. Hierarchical NP assemblies can be obtained using sublimation of LC material to fabricate transparent omniphobic surface. LC ligands can be used to achieve long range reversible close-packing of nanoparticles.[22] Closed-packed assemblies of NPs can be obtained in presence of LC topological defects. The release of the LC defect energy indeed allows for stabilization of the composite systems when NPs are confined in the defect cores.[23–28 29] LC topological defects may thus be used as a matrix for new kinds of NP organizations templated by the defect geometry[27,30,31] provided that the defects are well-oriented. This orientation can be achieved in smectic arrays of defects[32–34] or in artificial arrays of nematic disclinations.[35–37] Up to now mostly 1D defects have been used leading to NP chain formation.[4,5,38–40] However the signal originating from NP chains is highly anisotropic but quite weak. The number of NPs in the chains remains small[40,41] as well as the number of oriented 1D topological defects, either in artificial nematic disclinations[35–37] or in the so-called smectic oily streaks where it is estimated at about 6 per μm.[32] 2D defects are promising in this context for the confinement of a large number of NPs but the question arises if it is possible to avoid a disordering of the NP organizations as the one usually obtained by deposing a solution of NPs on a substrate.

Recently it has been shown that the 2D topological defects in the oily streaks of smectic 4-*n*-octyl-4'-cyanobiphenyl (8CB) allow for a 2D confinement of gold nanospheres and lead to the formation of 2D NP hexagonal networks.[41] In order to understand if and how an orientation can also be obtained at the macroscopic scale, we have compared two 8CB smectic structures, oily streaks with 1D (dislocations) and 2D defects (grain boundaries) and the so-called "large stripes" with *a priori* different kinds of 2D defects. We have analyzed networks of spherical NPs (gold nanoparticles - GNPs) and networks of rods NPs (CdSe/CdS dot-in-rods - DRs) in 8CB LC films. Combining optical microscopy, Rutherford Backscattering Spectrometry (RBS) measurements, Grazing Incidence Small Angle X-ray Scattering (GISAXS) and Transmission Small Angle X-ray Scattering (TSAXS), we reveal the crucial role of the smectic layers only present below the 2D topological defects of oily streaks that appear able to orient in the defects not only the DRs but even the networks of NPs.

2 Results and discussion

2.1 Two kinds of LC structures: oily streaks and large stripes

The 8CB film is deposited on top of rubbed polyvinyl alcohol (PVA) polymer substrate (see "Experimental section"). Its structure results from an antagonist anchoring at the substrate/film and film/air interfaces. The 8CB smectic molecules are parallel to the PVA rubbing and perpendicular to the 8CB-air interface (Fig. 1a and c). Due to this hybrid anchoring, the smectic layers become curved to yield flattened hemicylinders oriented along a single direction (Ox) as shown in the Fig. 1 ((Ox) is perpendicular to the unidirectional anchoring at the rubbed PVA substrate).[42] These flattened smectic hemicylinders can be detected by Polarizing Optical Microscopy (POM) pictures in reflection between crossed polarizers ((Oxy) plane - Fig. 1b and 1d), in relation with the corresponding lateral modulation of the projection of the extraordinary optical constants along the (Oy) direction. Parallel stripes are observed, each stripe corresponding to one flattened hemicylinder. We have prepared smectic films of different thickness ranging between 110 nm and 270 nm. Two different LC patterns are detected in POM which can be distinguished according to their periodicity. Firstly the one has a typical periodicity P between 0.5 μm and 1 μm (oily streaks[42–44]). Its internal structure

has been extensively studied using combined X-ray synchrotron scattering and ellipsometry measurements.[32,45] It is described in Fig. 1b, which displays a cross section-view ((Oyz) plane) of one given hemicylinder: in each hemicylinder, a sublayer of smectic layers perpendicular to the PVA substrate has been detected. A 2D central defect is then formed on the top of the sublayer, shown in green in Fig. 1b. It is a 2D grain boundary that connects the perpendicular layers in the sublayer and the flat layers above. It possibly corresponds to a locally melted 2D area, of width around 400 nm[32] and length equal to the sample length (18 mm). At the two edges of the hemicylinder around six edge linear dislocations (Fig. 1b in blue), which are 1D topological defects, are expected to be dispersed along two Rotating Grain Boundaries (RGB in red Fig. 1b).[32] Secondly, there is a different LC pattern shown on Fig. 1c. It is associated with larger stripes observed in POM pictures (Fig. 1d) of period *P'* varying between 1 μm and 3 μm.

We expect the same rotation of the smectic layers in the edges of the large stripe hemicylinders, including the presence of around six linear dislocations. However the central part of the hemicylinders of the large stripes becomes significantly larger suggesting the absence of the central grain boundary characteristic of oily streak hemicylinders whose energy cost would become prohibitive. The structure of the central part of the large stripes is however still unknown. It will be discussed later (see the "discussion" section, *SI Text* and Fig.SI 1). This is why it is marked with a "?" in Fig. 1d.

By controlling the distance between the PVA substrates and the rubbing roller of the rubbing machine, we are able to control effectively the proportion of the two kinds of patterns in the LC film. For shorter distances (strong rubbing forces), the oily streaks texture is generally the most stable texture, largely dominating the overall structure. The proportion of large stripes increases when increasing the distance substrate-roller (reducing the rubbing forces). For intermediate rubbing, both textures coexist. In this way, the confinement properties in presence of NPs of both oily streaks and large stripes can be compared.

2.2 NPs/LC composite films

To investigate the potential of the defects present in the hemicylinders, for tailoring optical properties at the nano-scale, we have investigated LC/NPs composite films with two types of NPs: Spherical GNPs that support Localized Surface Plasmon Resonances (LSPR) and CdSe/CdS DRs that emit polarized light.

2.2.1 Spherical gold nanoparticles (GNPs)

GNPs are of diameter 5 nm and covered by dodecanethiols as ligands ("Experimental section"). It is known that for low average GNP concentration, almost only GNP chains form, confined in the 1D defects.[4,38] At large concentration, when the 1D defects are almost fully filled, 2D GNP networks form.[41] POM pictures (Fig. 2a and Fig. 3a) with parallel polarizers display ribbon-like structures of larger brightness that can be identified as GNP ribbon-like assemblies parallel to the 8CB stripes. They form in both oily streaks (Fig. 3a) and large stripes (Fig. 2a). In order to compare the corresponding GNP organizations induced in oily streaks and large stripes, we have prepared a mixed composite film of average thickness 180 nm, covered by long GNP ribbon assemblies like the ones of Fig. 2a and 3a..

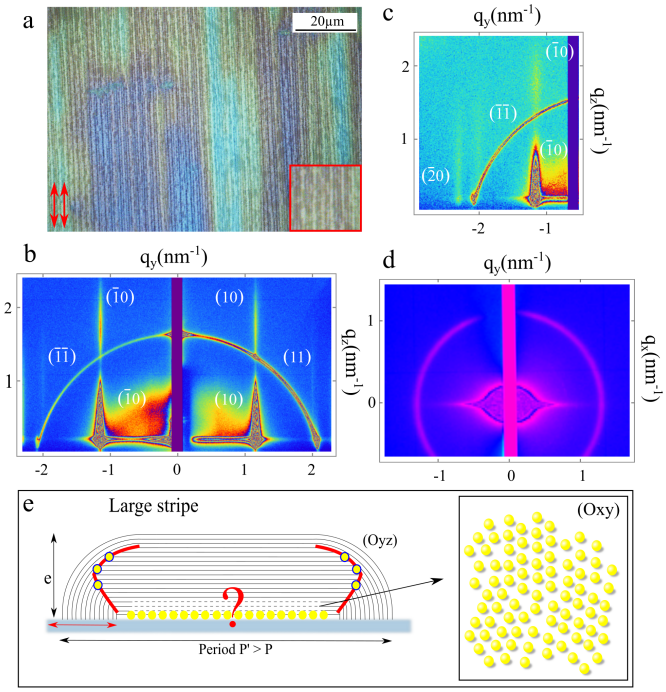

rx$_L$.*png*

Fig. 2 (a) POM picture between parallel polarizers of a GNPs composite film area mostly covered by large stripes with GNP concentration C_{avg} = 6900 GNPs μm^{-2} and average thickness $e_{avg} = 220$ nm locally varying between 180 nm and 230 nm. (b)-(c) GISAXS scattering pattern with two detector positions for a zone dominated by large stripes ($e_{avg} = 180$ nm, C_{avg} is between 5700 GNPs μm^{-2} and 7000 GNPs μm^{-2}). The GNP scattering rods are labelled in relation with an hexagonal GNPs assembly. (d) TSAXS scattering pattern of the same zone - the ring corresponds to the ((10), $(\bar{1}0)$) rods, with disordered orientations that could be similar to the scheme shown in (e).

Using the fact that the smectic texture does not change in the direction parallel to the stripes but it changes in the perpendicular direction, we obtain well-defined areas respectively mostly covered (by more than 80 %) with oily streaks (Fig. 3a) or mostly covered with large stripes (Fig. 2a). Each area is of length equal to the sample length in the direction parallel to the hemicylinders (18 mm) and of smaller width in the perpendicular direction, typically around 500 μm. POM investigation and RBS measurements allow to design a texture map of these areas. The average GNP concentration was ranging between 2000 GNPs μm^{-2} and 6900 GNPs μm^{-2} in oily streak areas and between 3500 GNPs μm^{-2} and 10700 GNPs μm^{-2} in large stripe areas.

This film has been measured by combined GISAXS and TSAXS in the SIXS - Soleil synchrotron beamline. The width of the X-ray beam was 300 μm and the incident angle for the GISAXS measurements was 0.25^o - See "Experimental section". Fig. 2b shows the GISAXS scattering pattern obtained when the propagation direction of the X-ray beam is parallel to the stripes on a zone of large stripes. The scattering half-circle observed on the 2D detector is associated with the scattering signal of the rotating 8CB smectic layers.[32] The detector was laterally translated along the

q_y direction (Fig. 2b and 2c) to confirm the presence of three symmetric pairs of diffraction rods ((10), $(\bar{1}0)$), ((11), $(\bar{1}1)$) and ((20), $(\bar{2}0)$). The q_z modulation of these rods is induced by the structural factor of the GNP spheres.[41] The respective q_y positions of the three pairs of diffraction rods are in the ratio 1, $\sqrt{3}$, 2 with $q_{(10)} = 1.16 \pm 0.01$ nm^{-1}. This shows that similarly to the case of GNP deposited on rubbed PVA without 8CB (Fig.SI 2a) there is formation of 2D GNP hexagonal networks. They are of period 6.3 nm slightly larger than the GNP diameter. The area associated with Fig. 2b and 2c has been analyzed through TSAXS measurement with the X-ray beam perpendicular to the stripes (Fig. 2d) - See "Experimental section". The signal of the rods ((10), $(\bar{1}0)$) in transmission exhibits a scattering ring. The same ring has been also observed for the GNP networks obtained without LC (Fig.SI 2b). This indicates that the GNP assemblies in large stripes are made of hexagonal meshes with different crystallographic orientations, in relation with a disorder of orientation for the 2D hexagonal network, that could correspond to a structure like the one schematized in Fig. 2e ((Oxy) plane).

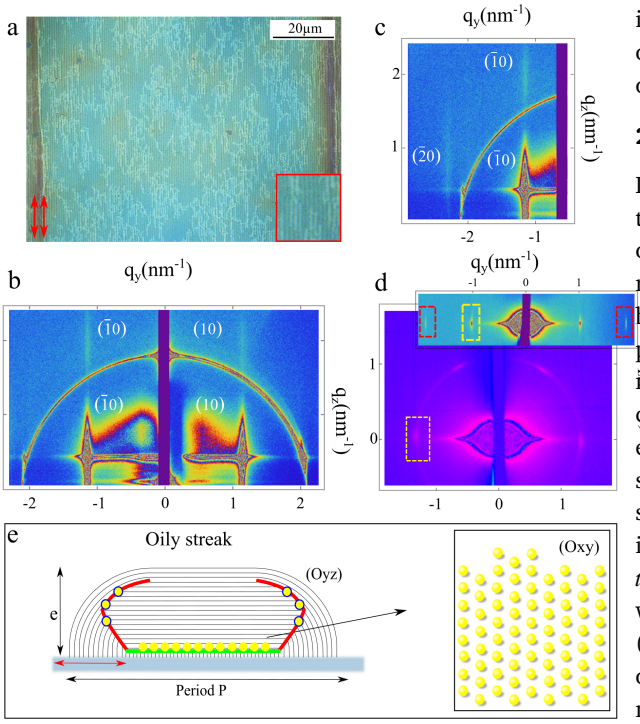

rx$_f$.*png*

Fig. 3 (a) POM picture between parallel polarizers of a GNPs composite film area mostly covered by oily streaks of local average thickness $e_{avg} =$ 175 nm and GNP concentration $C_{avg} = 3200$ GNPs μm^{-2}. (b)-(c) GISAXS scattering patterns with two detector positions for a zone dominated by oily streaks ($e_{avg} = 180$ nm, C_{avg} between 2700 GNPs μm^{-2} and 5100 GNPs μm^{-2}). The GNP scattering rods are labelled in relation with an hexagonal GNPs assembly. (d) TSAXS scattering pattern of the same zone ; the ((10), $(\bar{1}0)$) rods are associated with spots at 0°, 60°, 120° and 180°, that correspond to formation of hexagonal GNPs networks of fixed orientation like the one shown in (e). The zoom in the inset of (d) shows the TSAXS spots of ((10), $(\bar{1}0)$) at 0° and 180° underlined by yellow rectangle compared to the LC signal underlined by red rectangles.

The same measurement has been performed on the specific areas of the GNP composite film composed in large majority by oily streaks. The GISAXS rods have been measured as well but as shown by Fig. 3b and 3c, the ((11), $(\bar{1}1)$) diffraction rods are no longer observed. This areas has been measured by TSAXS, leading to the signal shown on Fig. 3d. The scattered ring is replaced by diffraction spots at 0°, 60°, 120° and 180°. This result is in agreement with the observation that only the ((10), $(\bar{1}0)$) and the ((20), $(\bar{2}0)$) diffraction rods are visible in GISAXS. It demonstrates that in the ribbons shown on Fig. 3a the GNP hexagonal network is oriented by the surrounding LC, when it is trapped in oily streaks, as schematized in Fig. 3e ((Oxy) plane). The dense $\langle 10 \rangle$ direction of the GNP network is parallel to the topological defects of the oily streaks, in other words perpendicular to the rubbing direction of the substrate. Zooming on the two spots at 0° and 180°, we also revealed the LC signal associated with the sublayer of smectic layers perpendicular to the rubbed PVA substrate and perpendicular to the rubbing direction (red rectangles - inset Fig. 3d). These smectic layers are localized at the bottom of the oily streak,[32] just below the central 2D defect (Fig. 1b), thus just below the GNP hexagonal assembly (Fig. 3e - (Oyz) plane). The comparison of the TSAXS signals evidences a similar width in the azimuthal direction for the two scattering signals, the one of GNP ((10), $(\bar{1}0)$) rods (yellow rectangles on Fig. 3d) and the one of LC perpendicular layers (red rectangles - inset Fig. 3d).

2.2.2 Fluorescent rod nanoparticles (DRs)

Does this orientation phenomenon transfers from spherical NPs to rod NPs independently of the different nature of the DRs and of the ligands ? We have studied fluorescent CdSe/CdS dot-in-rods (DRs) of diameter 7 nm and of length 22 nm (determined by Transmission Electron Microscopy (TEM)) and covered with phosphonic acid as ligand ("Experimental section"). Fluorescence microscopy reveals that, depending on the average surface concentration and similarly to GNPs (Fig.SI 3) DRs are organized either in short ribbons (Fig. 4a and 4b) or in large ribbon-like structures (Fig. 4c and 4d), both in oily streaks and in large stripes. Two different exposure times, t_{exp}, have been used to identify the different small spots of DRs, $t_{exp} = 8$ ms (Fig. 4a) and $t_{exp} = 1$ s (Fig. 4b). Fig. 4b with $t_{exp} = 1$ s shows that together with the short ribbons, thin fluorescent lines can be distinguished (underlined with circles and mapped on the POM picture in inset of Fig. 4b). Owing to the spatial resolution of the fluorescence microscopy, these thin fluorescent lines have a lateral extension of the order of two neighbouring quarters of cylinders. For each thin fluorescent line/ribbon shown in Fig. 4a-c, the number n of involved DRs per μm as well as the number N of the equivalent chains of closely packed DRs parallel to the POM stripes are determined using the emitted intensity of a single DR (see "Experimental section"). For the measured thin fluorescent lines like the ones shown on Fig. 4b, N varies between 4 and 6. This result is in agreement with the hypothesis of thin fluorescent lines associated with the 1D defects of two neighbouring quarters of cylinders filled by DRs. Fluorescent lines are then made of DR chains localized in a number of 1D defects that might vary between 1 and 6. In contrast fluorescent ribbons like the ones underlined with diamonds (oily streaks ribbons) and triangles (large stripes ribbons) in Fig. 4a and 4c, are systematically associated with N larger than

6 since n varies between 450 DRs and 1500 DRs and the number required to fully fill six 1D dislocations in one smectic hemicylinder is 258 DRs. The ribbons may be associated with the formation of 2D networks of DRs by analogy with the 2D networks revealed by GISAXS/TSAXS for nanospheres. We have analyzed the polarization of the photoluminescence intensity as a function of the analyzer orientation α, $\alpha = 0°$ corresponding to an orientation parallel to the hemicylinder stripes visible by POM. The intensity of the fluorescent lines appears to be well fitted by a $\cos^2(\alpha)$ function (Fig. 5a), as shown for line #1 and #2, respectively corresponding to oily streaks and large stripes (Fig. 4b). The intensity maximum (I_{max}) occurs for $\alpha = 0°[\pi]$. This result also holds for DR ribbons but only for oily streaks with a lower oscillation amplitude (see Fig. 5a for oily streak ribbon #3 - Fig. 4a. The intensity profile of the fluorescent ribbons localized in large stripes is indeed mostly constant with α and cannot be fitted by $\cos^2(\alpha)$ function (see ribbon #4, Fig. 5a - Fig. 4c). We have measured the degree of linear polarization $\delta = (I_{max} - I_{min})/(I_{max} + I_{min})$ (see "Experimental section") in the case of large stripes and oily streaks separately for both DR assemblies, fluorescent lines and ribbons. A statistical analysis is presented in Fig. 5b-e. For 49 DR fluorescent lines in oily streaks, the average value is $\delta = 0.64 \pm 0.15$ (Fig. 5b), quite similar to the one for 39 DR fluorescent lines in large stripes ($\delta = 0.6 \pm 0.13$ - Fig. 5d). For 53 DR ribbons trapped in oily streaks the average δ is 0.4±0.1 (Fig. 5c). This is lower than for DR chains but corresponds to DRs in average oriented along the 8CB hemicylinders. For 27 DR ribbons trapped in large stripes (Fig. 5e) the average δ is almost zero (0.08 ±0.09), suggesting that DR ribbons in large stripes are either made of DRs standing perpendicular to the substrate or made of flat randomly oriented DRs, this latter organization corresponding to the one observed when DRs are deposited on substrates without LC (Fig.SI 4a).

Based on this similarity, we can favour the hypothesis of this latter structure for the DR ribbons in large stripes and schematize the evolution of DR ribbons and chains as shown in Fig. 4e and 4f in the (Oxy) plane, respectively for oily streaks and large stripes when the DR concentration increases.

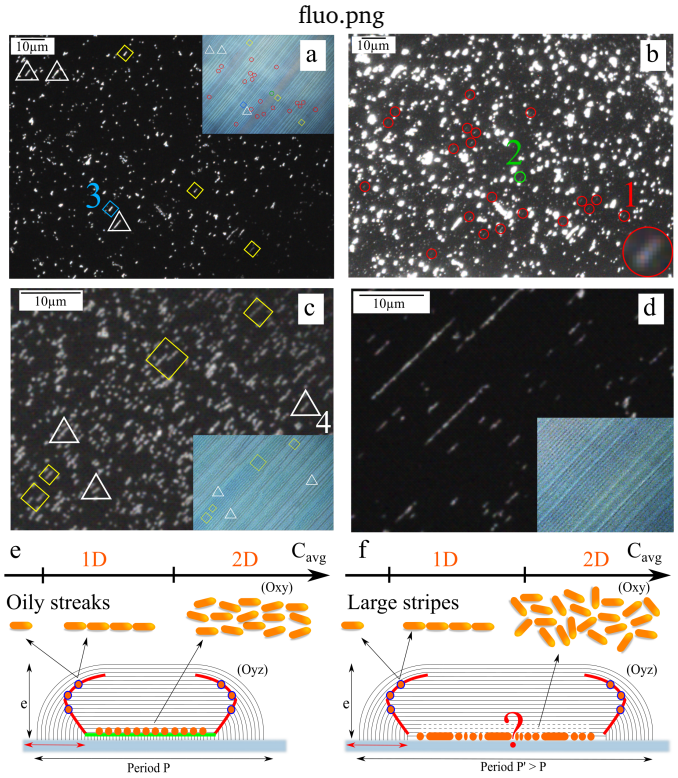

Fig. 4 Fluorescent microscopy pictures with in insets the corresponding POM pictures: (a)-(b) The same region of LC thickness $e = 170$ nm, taken with two different exposure times. (a) $t_{exp} = 8$ ms, showing short ribbons of DRs trapped in oily streaks (diamonds) and in large stripes (triangles). (b) $t_{exp} = 1$ s, showing fluorescent lines (underlined with circles and DR line #1 in the inset). (c) Region of local concentration $c_{avg} = 570$ DRs μm^{-2}, LC thickness $e = 220$ nm where DRs form denser domains of longer ribbons, taken with $t_{exp} = 4$ ms. (d) Region of local concentration $c_{avg} = 250$ DRs μm^{-2} and LC thickness $e = 170$ nm, taken with $t_{exp} = 4$ ms, showing long DRs ribbons. (e)-(f) Scheme of the evolution of the DRs organization from 1D to 2D assemblies, when the NPs concentration increases in oily streaks and large stripes respectively.

2.3 Discussion

The combined results on GNPs and DRs demonstrate that oily streaks in presence of topological defects not only confine NPs in specific localizations, but also induce an average orientation parallel to the topological defects for anisotropic DRs and NP networks. Two types of topological defects may be involved in these long-range organization:

- The 1D defects are able to confine NPs and allow for NP chain formation. It was known that spherical GNPs could form long chains in oily streaks.[4,41] We now evidence formation of chains that can occur for nanorods of different nature (gold nanorods[39] and CdSe/CdS dot-in-rods) and different ligands. With fluorescent nanorods we evidence that long chains can also be formed in both oily streaks and large stripes. Until 80% of the 6 expected dislocations can be filled as shown by the local number of DRs in the thin fluorescent lines (Fig. 4e and 4f). In the chains DRs remain almost perfectly oriented along the 8CB hemicylinders without any significant disorder induced by the large chain length. This is shown by the large degree of polarization, very similar to the one of single DRs.[5] A strict confinement is thus induced in smectic dislocations in relation with a dislocation core size of the same order as the rod diameter[5,40] with no significant distortion of the dislocations induced by the presence of a large number of DRs.

- A 2D grain boundary in oily streaks, separating the vertical smectic layers (bottom of the LC film) from the horizontal ones (top central part of the LC film) may confine NPs in 2D. This defect is expected of size of about 400 nm[32] which leads to the confinement of large NP ribbons that become easily observed by optical microscopy for GNPs (Fig. 3a) and by fluorescence microscopy for DRs (Fig. 4). As an example for the DR ribbon #3 shown on Fig. 4a of $n = 1440$ DRs per μm, a model of 2D side-by-side closed-packed DRs would lead to a ribbon of width around 200 nm, almost half the width of the expected 2D grain boundary defect of oily

de polarisation.png

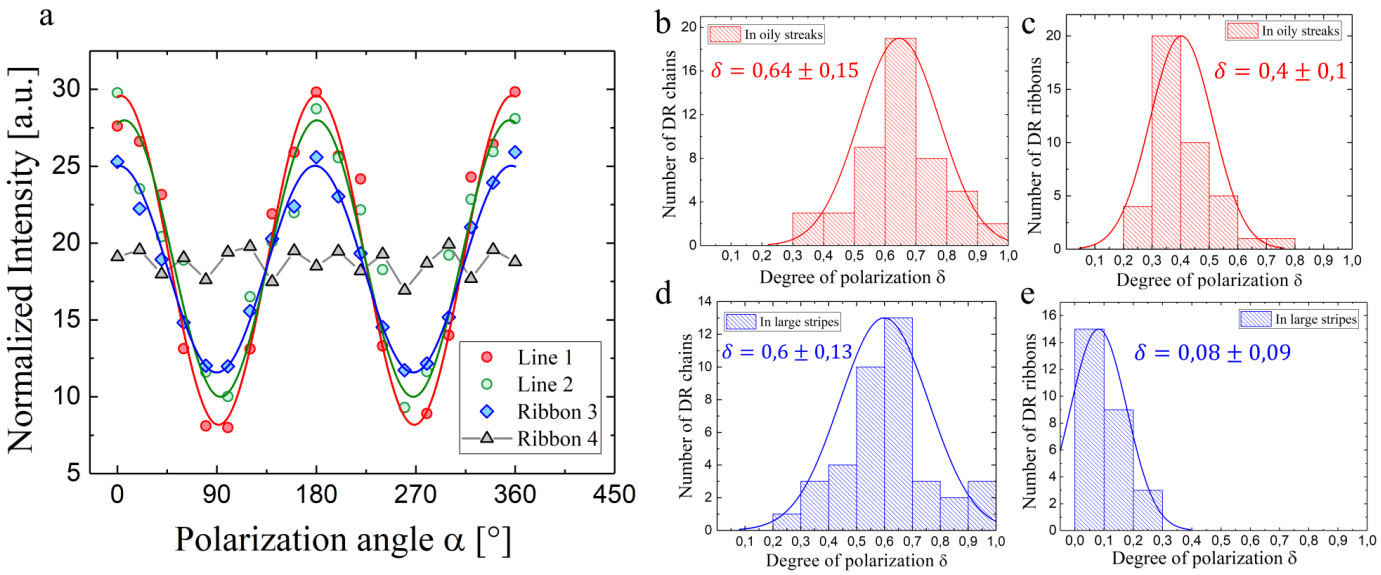

Fig. 5 (a) Evolution of the normalized photoluminescence intensities with the polarization angle α of DRs line #1, line #2, ribbon #3 and ribbon #4 observed on Figure 4. The intensity profiles of line #1, line #2 and ribbon #3 are first fitted with the function $I_{min} + (I_{max} - I_{min})\cos^2(\alpha)$, $\alpha = 0$ corresponding to the direction of the 8CB stripes. This allows to extract the value of the degrees of polarization ($\delta = (I_{max} - I_{min})/(I_{max} + I_{min})$). The curves are then offsetted to allow for a comparison on the same graph. The histograms of all measured degrees of polarization δ fitted by gaussians are presented for: (b) lines in oily streaks, (c) ribbons in oily streak, (d) lines in large stripes and (e) ribbons in large stripes.

streaks. This width is consistent with the 730 nm value obtained by fluorescence microscopy measurement that takes into account the size increasing induced by diffraction, of the order of 500 nm for the two sides of the ribbon. In these large ribbons an overall disorder for both DR orientation and NP network orientation could have been expected. This indeed happens on a substrate without LC (Fig.SI 2 and SI 4.a) when solvent evaporation is not controlled [14] and in large stripes (Fig. 2b-d,e, Fig. 4f and 5e). In contrast, in oily streaks DR orientation is not fully disordered and GNP hexagonal networks are oriented.

In oily streaks the average DR polarization degree of 0.4 for ribbons (Fig. 5c) shows that DRs are flat as expected if they would be confined in the core of the 2D grain boundary. In addition DRs are in average oriented parallel to the 8CB hemicylinders thus oriented along a unique direction defined by the rubbing of the substrate. This leads for large DR concentration to a sample made of fluorescent ribbons dispersed all over the LC film. Each ribbon is characterized by a large and polarized emission intensity, even though the polarization is less defined than for DRs in chains in obvious relation with the different kind of confinement. As a result, we can use these two kinds of oily streak topological defects to control the macroscopic polarization of the emitted photoluminescence of a large number of DRs organized both in long chains and in ribbons along a single direction. This DR orientation could be associated with a well-defined network of oriented DRs in the ribbons like the one schematized on Fig. 4e. This agrees with the well-defined scattering rods observed at $q_y = \pm 0.9$ nm^{-1} in GISAXS experiments for an oily streak zone of DRs composite film (Fig SI 5). It corresponds to a center-to-center distance between DRs of 8 nm, in agreement with close side-by-side packing of oriented DRs of diameter 7 nm, separated by interdigitated ligands. For GNPs, despite their isotropic shape, a well-defined hexagonal network strictly orientated by the oily streaks is induced (Fig. 3e). The dense direction of the GNP hexagonal network, i.e. the $\langle 10 \rangle$ direction, is parallel to the 8CB hemicylinders. It can be noticed in Fig. 3d that the remaining orientation disorder of the GNPs network is similar to the one of the perpendicular smectic layers close to the substrate. This suggests a coupling between the GNP network and the perpendicular smectic layers. The undulations of the perpendicular layers are induced by the not strictly straight rubbing of the PVA substrate and may be transmitted to the GNP hexagonal network which is formed directly on top of the perpendicular layers (Fig. 1b). The perpendicular layers are all parallel to the hemicylinder axes and might guide both the DR orientation and the dense directions of the ordered NP networks (the $\langle 10 \rangle$ direction for the GNP hexagonal network). A signature of this effect could be the significant absence of both DR orientation and GNP network orientation displayed by the large stripes. The observation of DR chains in large stripes confirms that the edges of the hemicylinders of large stripes may be similar to the oily streak ones. We can postulate that large stripes are smectic flattened hemicylinders where the central zone would include flat layers directly in contact with the substrate with no perpendicular layer below. This assumption is consistent with large stripes being induced by a local smoother rubbing of PVA that would correspond to a local weaker anchoring energy. Ellipsometric measurements performed on large stripes are indeed in reasonable agreement with a large stripe model including a proportion of 16% of flat layers directly in interaction with the rubbed PVA substrate (*SI*

Text and Fig.SI 1). NP ribbons are formed in the central zone of large stripes because they advantageously replace flat layers in direct interaction with the substrate by flat layers in interaction with ribbons of NPs. It is for example known that the dodecanethiol ligands of GNPs induce tilted or homeotropic anchoring and may transform NP ribbons into favorable areas for adsorbed flat smectic layers.[46] NP ribbons being formed directly on the substrate, a similar NP structure might be expected for NPs in large stripes (Fig. 2d) and for NPs deposited on the substrate without LC (Fig.SI 2b) in agreement with observations. This underlines the crucial role played by the perpendicular layers below the NP ribbons in driving the NP orientation within the oily streaks. A coupling may be induced between the smectic layers and the NP ligands. However the flat smectic layers on top of the central defect become on top of the NP ribbon which is confined in the defect, similarly to the flat layers of the large stripes that are on top of NPs themselves lying on the substrate. This suggests that the flexibility of the NP ligands allows for a different anchoring above and below the ribbons. We can then expect a variation of the guiding efficiency not only with the size and shape of NPs but also with the ligand nature.

3 Conclusion

We have demonstrated how the confinement induced by 1D smectic LC topological defects such as dislocations leads to the formation of NP chains and the confinement induced by 2D smectic LC topological defects such as smectic grain boundaries leads to the formation of 2D ribbons of NPs. Both are oriented along a single direction, the defect direction, for various NP shape, size, nature and ligands. Applying optical microscopy, RBS measurements and GISAXS/TSAXS to the smectic oily streaks which are arrays of 1D defects and 2D grain boundary defects, in presence of spherical GNPs and CdS/CdSe DRs, we show that not only the NP themselves are oriented in the ribbons when they are nanorods, but also the network of NPs: Fluorescent DRs (diameter 7nm, length 22nm) organize in ribbons that can be larger than 200 nm and longer than 10 μm. The ribbon polarization of light emission is parallel to the defects and characterized by a degree of polarization 0.67 times the one of single DRs or of DRs chains when they are trapped in 1D defects. This demonstrates that the DRs in the ribbons remain in average oriented along the defects with a disorder of orientation slightly larger than in DR chains. GNPs of diameter 5 nm self-assemble in 2D hexagonal networks of $\langle 10 \rangle$ direction strictly oriented along the defects. This is in contrast to similar smectic textures which do not include a 2D grain boundary but have flat smectic layers which may be in direct contact with the substrate instead of perpendicular smectic layers at the grain boundary. For GNPs they locally induce hexagonal NP order in the ribbons as well, but without any specific average orientations. They also do not orient DRs. The orienting role of the perpendicular smectic layers below the grain boundary appears crucial. It is likely driven by the ligands arounds NPs that may be able to change their geometry depending on the smectic layers in contact with the ribbons, either flat or perpendicular to the ribbons. The guiding process of the smectic layers below the grain boundaries, allowing for the creation of a large number of oriented ribbons, made of more than 1000 NPs μm^{-2}, opens the route for highly anisotropic optical properties of the composite films. This is promising not only for anisotropic optical properties, like plasmonic absorption of metallic NPs controlled by polarization or polarized emission of quantum dots, but even more interestingly for collective behaviors that could emerge in relation with the close packing of NPs in well-ordered networks in the ribbons.

4 Experimental Section

4.1 Nanoparticles synthesis

4.1.1 Chemicals

For CdSe/CdS NRds: Cadmium oxide (CdO) (Sigma Aldrich 99.99%), sulfur powder (S, Afla Aesar, 99.5%), selenium powder (Strem Chemicals, 99.99%), Trioctylphosphine oxide (TOPO 99%), trioctylphosphine (TOP, Sigma-Aldrich, 97%), Octadecylphosphonic acid (ODPA, TCI 99%), hexylphosphonic acid - (HPA, TCI 99%), Chloroform (Carlo Erba), ethanol absolute anhydrous (Carlo Erba, 99.9%), methanol (Carlo Erba, 99.8%), acetone (Carlo Erba, 99.8%), n-hexane (Carlo Erba), n-octane (SDS, 99%), toluene (Carlo Erba, 99.3%) and n-octane (SDS, 99%).
For Gold NPs: Chlorotriphenylphosphine gold ÄšI) and tert-butylamine borane (STEM chemicals), Dodecanethiol (Sigma-Aldrich), toluene (Riedel de Haen,98%) and ethanol (Prolabo,99.8%). All reagents were used as received without further purification.

4.1.2 Synthesis of CdSe seeds

In a 100 mL three neck flask, CdO (60 mg) with ODPA (0.3 g) and TOPO (3 g) are degazed under vacuum at 125 ^{o}C for 15 minutes. The atmosphere is switched to Ar and the temperature raised to 300 ^{o}C, until the solution gets clear. The solution is then cooled down and then degased for another 10 min. The atmosphere is switched to Ar and the temperature raised to 380 ^{o}C. TOP (1.5 g) is added and we wait for the vacuum to recover. Meanwhile, sonicate Se powder (58 mg) with TOP (0.36 g) until a clear transparent solution is obtained. This TOPSe solution is quickly injected. The heating mantle is immediately removed. At this stage the solution is dark red, with a white PL. After cooling, the solution present a green PL, peaked at 566 nm. The solution is cleaned twice using toluene as good solvent and ethanol as non solvent.

4.1.3 Synthesis of CdSe/CdS dot-in-rod

In a 100 mL three neck flask, CdO (86 mg) with HPA (90 mg), ODPA (0.28 g) and TOPO (3 g) are degazed under vacuum at 150 ^{o}C. The atmosphere is switched to Ar and the temperature raised to 300 ^{o}C until a clear solution is obtained. The flask is then cooled just above 100 ^{o}C and degazed again. The atmosphere is switched to Ar and the temperature raised to 350 ^{o}C. TOP (1.5 g) is then added. Meanwhile, mix S powder (120 mg) with TOP (1.5 g) until a clear yellowish solution is obtained. Inject simultaneously and promptly the TOPS solution and the CdSe core (0.4 mL, 200 μM). The reaction is continued for 9 min. Then the heating mantle is removed and the flask cooled down using fresh air. The solution is cleaned twice using toluene as good solvent and

ethanol as non solvent. The solution is stored in toluene (8 μM). The Photoluminescence peak appears at 598 nm and presents an orange color (Fig.SI 4b).

4.1.4 Synthesis of Gold nanospheres

The synthesis of gold NP is carried out in a glove box by using oil bath for heating. In a flask (50 mL), chlorotriphenylphosphine Au(I) (124 mg) is dissolved in toluene (25 mL) at 100 °C. After total dissolution of precursor, dodecanethiol (500 μL) is added to the solution. Tert-butylamine borane complex (434 mg) is dissolved in a tube with toluene (2 mL) at 100 °C. When the two solutions are optically clear, tert-butylamine borane is added to the gold precursor solution. The colorless and clear mixture turns slowly to brown and reach a dark red solution. For the watching step, the NP solution is dried under nitrogen flux and ethanol (9 mL) is added to the black powder. After centrifuging, the black precipitate is redispersed in toluene. To remove the impurities, the solution is centrifuged again and the remaining precipitated is discarded. The obtained GNPs are of diameter 5 nm, determined by Small Angle X-ray Scattering (SAXS).

4.2 Sample preparation

The poly(vinyl alcohol) (PVA from Sigma Aldrich) thin layer was prepared by spin-coating droplet (100 μL) of an aqueous solution of PVA (0.5 wt %, acceleration 400 rpm s^{-1}, speed 3000 rpm, during 30 s) on glass slides of surface 18 mm×18 mm. Right before spreading the LC film, the PVA layer was firstly heated at the oven for 1 hour at 140 °C. Secondly, it was rubbed by using a rubbing machine to impose a unidirectional anchoring to the LC molecules. The distance between the stage and the roller was chosen precisely to control the rubbing forces. The LC films are then obtained by spin-coating droplets (50 μL, 0.2 M) of 4-*n*-octyl-4'-cyanobiphenyl (8CB from Sigma-Aldrich) in toluene as solvent (speed 3000 rpm during 30 s, acceleration between 500 rpm s^{-1} and 1000 rpm s^{-1}) on the rubbed PVA substrate. The same protocol is used to prepare LC/NPs composite samples by mixing the 8CB solution with the NPs solution, using different NP concentrations, depending on the samples. The film thickness ranges between 110 nm and 270 nm when the spin-coating acceleration varies between 500 rpm s^{-1} and 1000 rpm s^{-1}. Samples of NPs without LC are obtained by spincoating droplets of the NPs colloidal dispersion on the PVA substrate. In order to obtain sample with individual dispersed DRs, a very diluted solution is used.

4.3 Optical and fluorescent microscopy techniques

Thin films were observed with an upright optical microscope (Leica DMRX) using either halogen lamp (brand band visible illumination) or a Prior lumen 200 lamp (for broad band UV and visible illumination). The light then goes through a dichroic mirror, which let UV-blue light excite the sample and filters out this contribution at the wavelength where nanocrystals emit. The emitted light was collected by a SONY CDD camera of resolution 1600 x 1200 pixels. LC or LC/NPs composite films are studied in reflection mode. With visible light between crossed polarizers the alternating bright and dark stripes correspond to domains containing molecules almost parallel or perpendicular to the substrate respectively (Fig. 1b-d). Between parallel polarizers, the colors are associated with interference phenomena induced by the interfaces of the LC film. The film thickness is thus extracted through the analysis of the Newton tints. For such a purpose we have established an abacus using an average optical index $n = (n_e + 2n_o)/3$, with $n_e = 1.67$, the extraordinary index and $n_o = 1.52$ the ordinary index. The UV-light was used to detect the fluorescent DRs, with a 590 nm filter to eliminate the reflection of the LC while allowing the photoluminescence signal from the DRs to get through (wavelength of 600 nm - Fig.SI 4b). To analyse the polarisation of the photoluminescence intensity of each DR assemblies (chains/ribbons), a rotating linear polarizer was placed at the output of the emitted light. The polarization rotation angle α was fixed at $\alpha = 0°$ when the polarizer is parallel to (Ox), the smectic hemicylinders axis (visible by POM). The polarized emitted light was then measured when rotating α with a pitch of 20° between $\alpha = 0°$ and $\alpha = 360°$.

4.4 DRs fluorescence Intensity

The fluorescence intensity measurements were analyzed using ImageJ, the free image processing program for both single DRs and DR assemblies (DR chains and ribbons). The fluorescent images were first transformed to 8-bit grayscale images then the *Integrated Intensity Density IntDen* is measured. It corresponds to the product of the selected area and the *Mean Gray Value* (the sum of the gray values of all the pixels in the selection divided by the number of pixels). First, $InDen_{R_1}$ of the selected region R_1 that includes the DR or the DR assembly, is determined. Second, $InDen_{noise}$ the corresponding background intensity is deduced from the product of the area of R_1 and the *Mean Gray Value* of a nearby "empty" region R_2, that contains no DR nor DR assembly. Finally the intensity I_{DR} of a single DR or the intensity I of a DR assembly is determined by subtracting $InDen_{noise}$ from $InDen_{R_1}$. It has been shown that there is no influence of the LC birefringence on the photoluminescence polarization anisotropy of the DRs.[5,47–52] Therefore, the fluorescence emitted intensity of single DRs has been measured using samples without LC. For each exposure time of the camera, an image sequence of 5 single DRs has been measured. For each image sequence, the average intensity of the single DR has been determined leading to the dependence of the single DR intensity on the camera exposure time t_{exp} shown on Fig. 6: $I_{DR} = 621(\pm 22) \times t_{exp}$. To obtain the number of DRs in each DR assembly in the LC composite film, we then divide the intensity I of a DR assembly by I_{DR} times the exposure time. For polarized intensity measurements, the same selected region, where DR assemblies are detected, was fixed while rotating the polarizer (angle α). Using the same method previously outlined, the polarized intensities were determined for all polarization angles α. To calculate the degree of polarization $\delta = (I_{max} - I_{min})/(I_{max} + I_{min})$ of each DR assembly, I_{max} and I_{min} are deduced from the polarization analysis curves that are well fitted by $I(\alpha) = I_{min} + (I_{max} - I_{min})\cos^2(\alpha)$. In Fig. 5a, the polarized intensities were normalized per unit of area in a second step

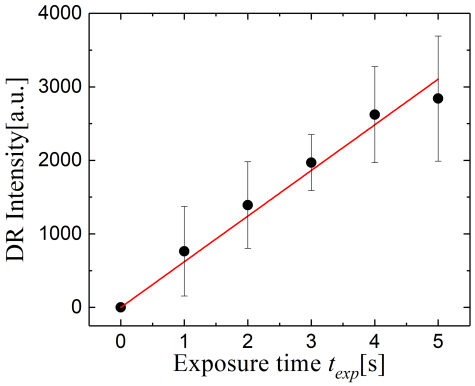

intensity.png

Fig. 6 Dependence of the single DR intensity per pixel on the exposure time t_{exp} with the red linear fitting :$I_{DR} = 621(\pm 22) \times t_{exp}$. Each mark corresponds to the average of about 5 independent measurements..

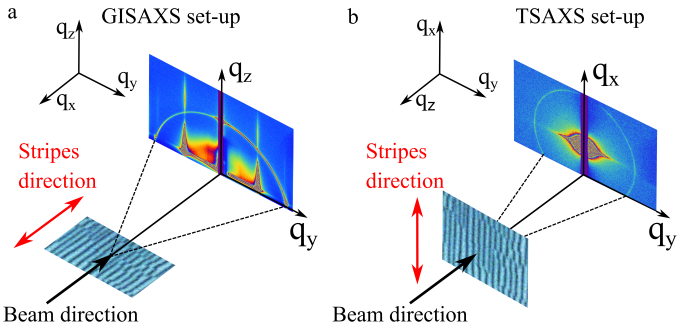

Fig. 7 X-ray set-ups with images of scattering signals on the Eiger detector: (a) Grazing Incidence Small Angle X-ray Scattering (GISAXS) showing LC scattering ring and NPs rods. (b) Transmission Small Angle X-ray Scattering (TSAXS) showing the NPs ring associated with the ((10), ($\bar{1}$0)) rods in GISAXS.

to allow for a comparison of all curves in a same graph.

4.5 Ellipsometry measurements

The full polarimetric properties of large stripes have been measured using a multimodal imaging Mueller polarimetric microscope. The measurements were made at a wavelength of 630 nm (filtered diode) in reflection mode with a $\times$50 microscope objective having a Numerical Aperture of 0.85. The Mueller matrix elements are presented using a conoscopic projection. The measurements were made by projecting the Fourier plane of the microscope objective on the imaging camera. In Fig.SI 1a and SI 1b, the radial position corresponds to angles of incidence θ comprised between normal incidence (centre of each element) and 58.5° (outer ring of each element). The polar angle ϕ corresponds to the orientation of the plane of incidence with respect to the axis of the large stripes. In our case, the large stripes were oriented horizontally.

4.6 X-Ray scattering measurements

The X-ray scattering measurements were performed at the SIXS beamline on the SOLEIL Synchrotron facility. The X-ray beam size is fixed at 300 μm $\times$ 300 μm with a photon energy of 18.44 keV. The scattering signal is observed on the 2D Eiger detector located at 1700 mm from the sample. Two different set-ups are used. The first (Fig. 7a) at a grazing incidence (GISAXS) where the incident beam is parallel to the smectic stripes probing an area of 300 μm width of the film and length of 18 mm (equal to the sample size). In Fig. 7a, the scattering ring is associated to the smectic hemicylinders while the scattering rods are related to the NPs organization in LC. The second set-up correspond to a transmission geometry (TSAXS) where the sample is rotated by 90° to become perpendicular to the incident beam that probes a local area of 300 μm $\times$ 300 μm. The detected signal becomes then associated to the wave vector $\boldsymbol{q}$ parallel to the interface (Fig. 7b).

4.7 Rutherford Backscattering Spectrometry (RBS) measurements

RBS measurements were carried out on the SAFIR platform of Sorbonne University. A 100 nA 2 MeV beam of $^4He^+$ was directed from the Van de Graaff accelerator onto the sample in a 0.5 mm beamspot for a total incident integrated charge of 10 μC. The backscattered ions were detected at 165° in a PIPS detector placed 7 cm from the beam impact point and collimated with a 2×0.5 mm window. Repeated measurements on a given point showed no loss of gold under the beam. The system was calibrated using a reference sample of 5.66×10^{15} Bi cm^{-2} implanted at 20 keV into silicon.

Author Contributions

Conceptualization, investigation, methodology, project administration and visualization: H. J. and E. La.; Funding acquisition and supervision: E. La.; Data curation: H. J., C. S., J. D. N., B. G. and D. C.; Formal analysis: H. J., C. S. and A. M; resources: E. La., A. V., A. C., Y. G., I. V., S. R., N. G. and E. L.; software: B. C., Y. G., J. D. N. and C. S.; Validation: E. La., D. B., Y. G. and B. G.; writing original draft: H. J.; Writing review and editing: H. J., E. La., M. G., B. G., D. B. and A. V. All authors have read and agreed to the published version of the manuscript.

Conflicts of interest

There are no conflicts to declare.

Acknowledgements

We thank Synchrotron SOLEIL for providing the beam on SIXS beamline and particulary B. Voisin and all the HERMES beamline members for the technical support. We also acknowledge the help of E. Briand for RBS measurements, the help of D. Limagne for the X-ray set-up and the help of Y. Prado for the sample preparation. We finally thank A. Soni for the graphical assistance.

References

1 J. Perez-Juste, I. Pastoriza-Santos, L. M. Liz-Marzan and P. Mulvaney, Coord. Chem. Rev., 2005, **249**, 1870–1901.

2 R. Krahne, G. Morello, A. Figuerola, C. George, S. Deka and L. Manna, Phys. Rep., 2011, **501**, 75–221.

3 N. J. Halas, S. Lal, S. Link, W.-S. Chang, D. Natelson, J. H. Hafner and P. Nordlander, Adv. Mat., 2012, **24**, 4842–4877.

4 D. Coursault, J. Grand, B. Zappone, H. Ayeb, G. Lévi, N. Félidj and E. Lacaze, Advanced Materials, 2012, **24**, 1461–1465.

5 L. Pelliser, M. Manceau, C. Lethiec, D. Coursault, S. Vezzoli, G. Leménager, L. Coolen, M. DeVittorio, F. Pisanello, L. Carbone et al., Advanced Functional Materials, 2015, **25**, 1719–1726.

6 M. Mayer, P. L. Potapov, D. Pohl, A. M. Steiner, J. Schultz, B. Rellinghaus, A. Lubk, T. A. F. Konig and A. Fery, Nano Letters, 2019, **19**, 3954–3862.

7 X. Li, J. Lyu, C. Goldmann, M. Kociak, D. Constantin and C. Hamon, J. Phys. Chem. Lett., 2019, **10**, 7093–7099.

8 J. Liu, L. Guillemeney, B. AbÃľcassis and L. Coolen, Nano Letters, 2020, **20**, 3465–3470.

9 C. Hanske, M. Tebbe, C. Kuttner, V. Bieber, V. V. Tsukruk, M. Chanana, T. A. F. Konig and A. Fery, Nano Lett., 2014, **14**, 6863–6871.

10 X. Ye, C. Zhu, P. Ercius, S. N. Raja, B. He, M. R. Jones, M. R. Hauwiller, Y. Liu, T. Xu and A. P. Alivisatos, Nature Com., 2015, **6**, 10052.

11 K. C. Elbert, D. Jishkariani, Y. Wu, J. D. Lee, B. Donnio and C. B. Murray, Chemistry of Materials, 2017, **29**, 8737–8746.

12 D. García-Lojo, E. Modin, S. Gómez-Graña, M. Impéror-Clerc, A. Chuvilin, I. Pastoriza-Santos, J. Pérez-Juste, D. Constantin and C. Hamon, Advanced Functional Materials, 2021, **31**, 2101869.

13 C. Hamon, M. Postic, E. Mazari, T. Bizien, C. Dupuis, P. Even-Hernandez, A. Jimenez, L. Courbin, C. Gosse, F. Artzner et al., ACS nano, 2012, **6**, 4137–4146.

14 B. T. Diroll, N. J. Greybush, C. R. Kagan and C. B. Murray, Chemistry of Materials, 2015, **27**, 2998–3008.

15 Y. Liang, Y. Xie, D. Chen, C. Guo, S. Hou, T. Wen, F. Yang, K. Deng, X. Wu, I. I. Smalyukh et al., Nature communications, 2017, **8**, 1–8.

16 V. Flauraud, M. Mastrangeli, G. D. Bernasconi, J. Butet, D. T. Alexander, E. Shahrabi, O. J. Martin and J. Brugger, Nature nanotechnology, 2017, **12**, 73–80.

17 C. Matricardi, C. Hanske, J. L. Garcia-Pomar, J. Langer, A. Mihi and L. M. Liz-Marzan, ACS Nano, 2018, **12**, 8531–8539.

18 D. S. Kim, A. Suh, S. Yang and D. K. Yoon, Journal of colloid and interface science, 2018, **513**, 585–591.

19 Q. Liu, Y. Yuan and I. I. Smalyukh, Nano letters, 2014, **14**, 4071–4077.

20 L. Jiang, H. Mundoor, Q. Liu and I. I. Smalyukh, ACS nano, 2016, **10**, 7064–7072.

21 H. Mundoor and I. I. Smalyukh, Small, 2015, **11**, 5572–5580.

22 W. Lewandowski, T. Aojewska, P. Szustakiewicz, J. Mieczkowski and D. Pociecha, Nanoscale, 2016, **8**, 2656–2663.

23 H. Yoshida, Y. Tanaka, K. Kawamoto, H. Kubo, T. Tsuda, A. Fujii, S. Kuwabata, H. Kikuchi and M. Ozaki, Applied physics express, 2009, **2**, 121501.

24 E. Karatairi, B. Rožič, Z. Kutnjak, V. Tzitzios, G. Nounesis, G. Cordoyiannis, J. Thoen, C. Glorieux and S. Kralj, Physical Review E, 2010, **81**, 041703.

25 B. Rožič, V. Tzitzios, E. Karatairi, U. Tkalec, G. Nounesis, Z. Kutnjak, G. Cordoyiannis, R. Rosso, E. G. Virga, I. Muševič et al., The European Physical Journal E, 2011, **34**, 1–11.

26 B. Senyuk, J. S. Evans, P. J. Ackerman, T. Lee, P. Manna, L. Vigderman, E. R. Zubarev, J. van de Lagemaat and I. I. Smalyukh, Nano letters, 2012, **12**, 955–963.

27 J. S. Evans, P. J. Ackerman, D. J. Broer, J. van de Lagemaat and I. I. Smalyukh, Physical Review E, 2013, **87**, 032503.

28 G. Cordoyiannis, V. S. R. Jampani, S. Kralj, S. Dhara, V. Tzitzios, G. Basina, G. Nounesis, Z. Kutnjak, C. S. P. Tripathi, P. Losada-Pérez et al., Soft matter, 2013, **9**, 3956–3964.

29 D. S. Kim, A. Honglawan, S. Yang and D. K. Yoon, ACS applied materials & interfaces, 2017, **9**, 7787–7792.

30 M. A. Gharbi, S. Manet, J. Lhermitte, S. Brown, J. Milette, V. Toader, M. Sutton and L. Reven, ACS nano, 2016, **10**, 3410–3415.

31 H. Mundoor, G. H. Sheetah, S. Park, P. J. Ackerman, I. I. Smalyukh and J. van de Lagemaat, ACS nano, 2018, **12**, 2580–2590.

32 D. Coursault, B. Zappone, A. Coati, A. Boulaoued, L. Pelliser, D. Limagne, N. Boudet, B. H. Ibrahim, A. De Martino, M. Alba et al., Soft Matter, 2016, **12**, 678–688.

33 I. Nemitz, I. Gryn, N. Boudet, R. Lemieux, M. Goldmann, B. Zappone, R. Petschek, C. Rosenblatt and E. Lacaze, Soft matter, 2018, **14**, 460–469.

34 R. S. Preusse, E. R. George, S. A. Aghvami, T. M. Otchy and M. A. Gharbi, Soft Matter, 2020, **16**, 8352–8358.

35 J.-B. Fleury, D. Pires and Y. Galerne, Phys. Rev. Lett., 2009, **103**, 267801.

36 B. S. Murray, R. A. Pelcovits and C. Rosenblatt, Phys. Rev. E, 2014, **90**, 052501.

37 M. Wang, Y. Li and H. Yokoyama, Nature Com., 2017, **8**, 1–7.

38 D. Coursault, J.-F. Blach, J. Grand, A. Coati, A. Vlad, B. Zappone, D. Babonneau, G. Lévi, N. Félidj, B. Donnio et al., ACS nano, 2015, **9**, 11678–11689.

39 B. Rozic, J. Fresnais, C. Molinaro, J. Calixte, S. Umadevi, S. Lau-Truong, N. Felidj, T. Kraus, F. Charra, V. Dupuis et al., ACS nano, 2017, **11**, 6728–6738.

40 S.-P. Do, A. Missaoui, A. Coati, A. Resta, N. Goubet, S. Royer, G. Guida, E. Briand, E. Lhuillier, Y. Garreau, D. Babonneau, M. Goldmann, D. Constantin, B. Croset, B. Gallas and E. Lacaze, Frontiers in Physics, 2020, **7**, 234.

41 S.-P. Do, A. Missaoui, A. Coati, D. Coursault, H. Jeridi, A. Resta, N. Goubet, M. M. Wojcik, A. Choux, S. Royer et al., Nano Letters, 2020, **20**, 1598–1606.

42 J.-P. Michel, E. Lacaze, M. Goldmann, M. Gailhanou, M. De Boissieu and M. Alba, Physical review letters, 2006, **96**, 027803.

43 J. M. Ok, Y. H. Kim, H. S. Jeong, H.-W. Yoo, J. H. Kim, M. Srini-

vasarao and H.-T. Jung, Soft Matter, 2013, **9**, 10135–10140.
44 B. Zappone and E. Lacaze, Physical Review E, 2008, **78**, 061704.
45 D. Coursault, B. H. Ibrahim, L. Pelliser, B. Zappone, A. De Martino, E. Lacaze and B. Gallas, Optics express, 2014, **22**, 23182–23191.
46 R. A. Drawhorn and N. L. Abbott, J. Phys. Chem., 1995, **99**, 16511–16515.
47 K.-J. Wu, K.-C. Chu, C.-Y. Chao, Y.-F. Chen, C.-W. Lai, C.-C. Kang, C.-Y. Chen and P.-T. Chou, Nano Letters, 2007, **7**, 1908–1913.
48 S. Burylov and Y. L. Raikher, Physics Letters A, 1990, **149**, 279–283.
49 S. V. Burylov and Y. L. Raikher, Physical Review E, 1994, **50**, 358.
50 M. Mukhina, V. Danilov, A. Orlova, M. Fedorov, M. Artemyev and A. Baranov, Nanotechnology, 2012, **23**, 325201.
51 A. Rodarte, C. Ferri, C. Gray, L. Hirst and S. Ghosh, Emerging Liquid Crystal Technologies VII, 2012, p. 82790H.
52 H.-S. Chen, C.-W. Chen, C.-H. Wang, F.-C. Chu, C.-Y. Chao, C.-C. Kang, P.-T. Chou and Y.-F. Chen, The Journal of Physical Chemistry C, 2010, **114**, 7995–7998.